Article | Received 21 February 2026; Revised 13 April 2026; Accepted 14 April 2026; Published 20 May 2026
https://doi.org/10.55092/aimat20260006

High-precision automated nanoparticle segmentation using a deep learning framework with boundary-aware and attention networks

Xiao Han[1,2], Linfeng Jin[3,*], Yijun Zhong[1,2,*] and Changfa Guo[1,2,*]

[1] Key Laboratory of the Ministry of Education for Advanced Catalysis Materials, College of Chemistry and Materials Science, Zhejiang Normal University, Jinhua 321004, China
[2] Zhejiang Key Laboratory of Advanced Catalysis and Adsorption Materials, College of Chemistry and Materials Science, Zhejiang Normal University, Jinhua 321004, China
[3] Department of Physics, College of Physics and Electronic Information Engineering, Zhejiang Normal University, Jinhua 321004, China

* Correspondence authors; E-mails: jlf@zjnu.cn (L.J.); yjzhong@zjnu.edu.cn (Y.Z.); changfa.guo@zjnu.edu.cn (C.G.).

1. Supplementary figures

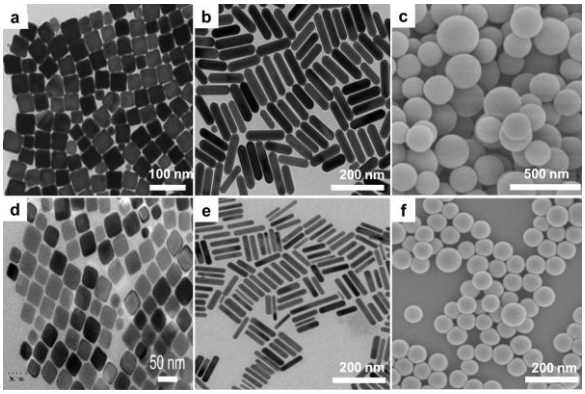

Figure S1. Representative electron microscopy images of nanoparticles in the dataset constructed in this study. **(a)** TEM image of ordered CuPd nanocubes synthesized with different amounts of 1,2-TDD (0.1 mmol) [1]; **(b)** TEM image of gold nanorods synthesized using a seed solution amount of 0.04 [2]; **(c)** SEM image of PFA nanospheres synthesized under the conditions of "PSA (2.8)–SDS (1.4)–FA (5.0)" [3]. Reprinted with permission. Copyright 2023 American Chemical Society; **(d)** TEM image of Cu nanocubes [1]; **(e)** TEM image of gold nanorods synthesized using a seed solution amount of 0.16 [2]; **(f)** SEM image of PFA nanospheres obtained after 4 h of reaction under FA acid catalysis in the presence of SDS [3]. Reprinted with permission. Copyright 2023 American Chemical Society. Due to layout constraints, these images were cropped proportionally, and the scale bars were redrawn according to the original image scale.

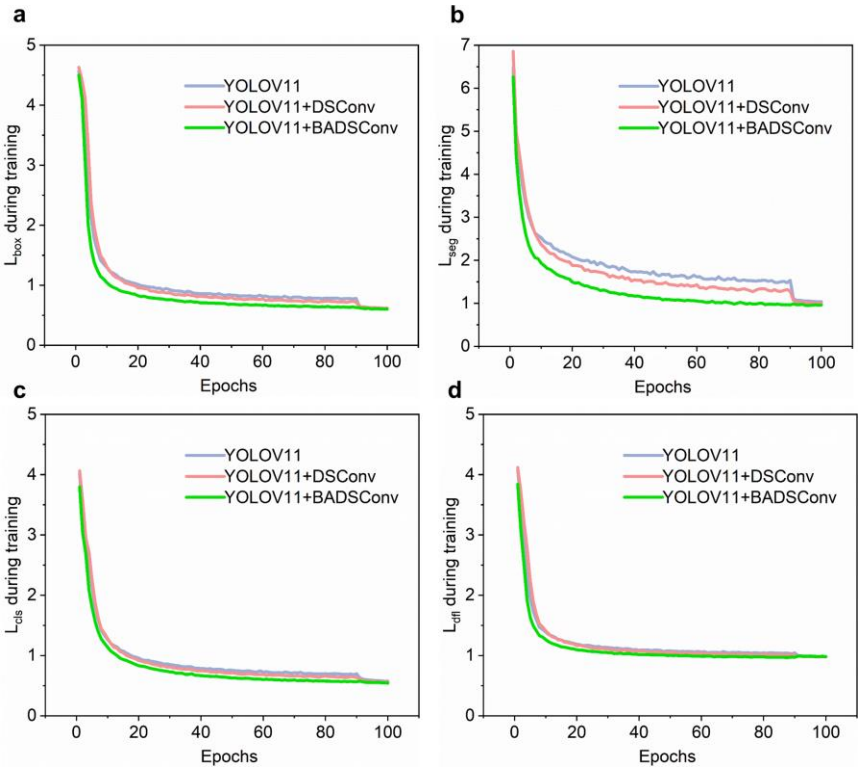

Figure S2. Training loss curves of YOLOV11, YOLOV11 with DSConv and YOLOV11 with BADSConv: **(a)** L_{box}; **(b)** L_{seg}; **(c)** L_{cls}; and **(d)** L_{dfl}.

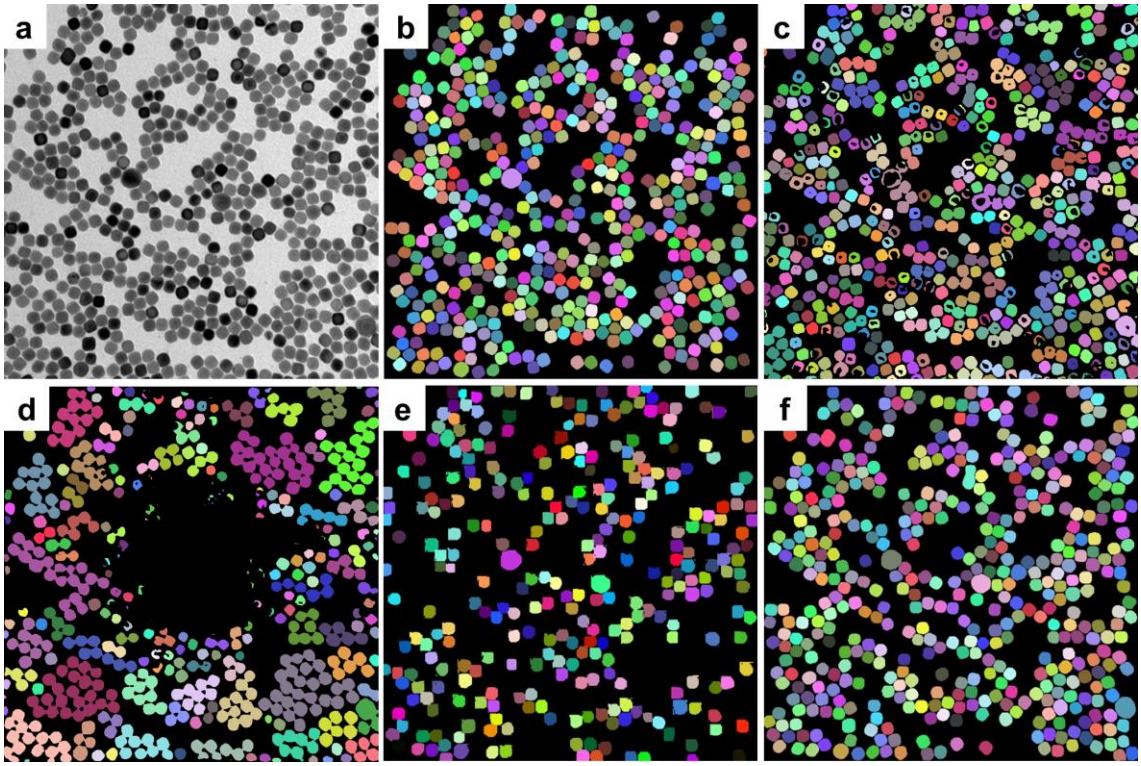

Figure S3. Visual comparison of segmentation results produced by different models: **(a)** TEM image of the Ag nanocubes [4]. Reprinted with permission. Copyright 2013 American Chemical Society; **(b)** Ground-truth annotation; **(c–f)** Segmentation results generated by U-Net, DeepLabV3+, YOLOv11, and NSYOLO, respectively.

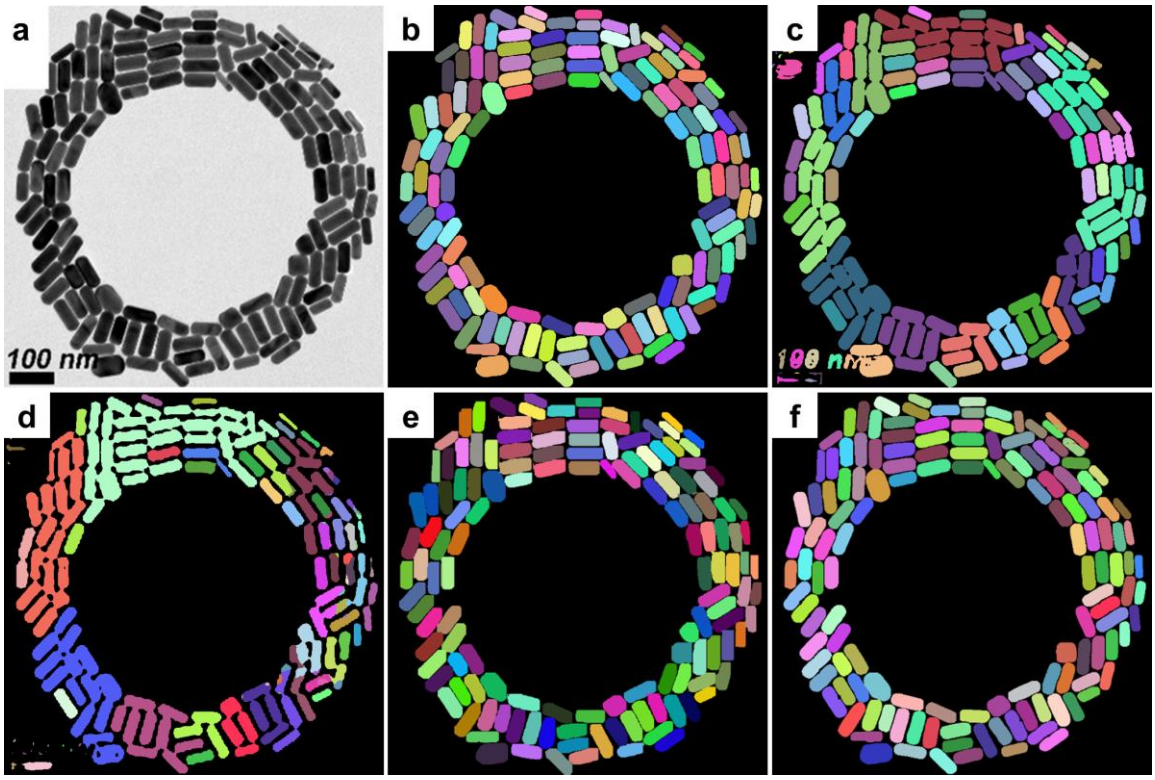

Figure S4. Visual comparison of segmentation results produced by different models: **(a)** TEM image of the Au nanorods [5]. Reprinted with permission. Copyright 2022 American Chemical Society; **(b)** ground-truth annotation; and **(c–f)** Segmentation results generated by U-Net, DeepLabV3+, YOLOv11, and NSYOLO, respectively.

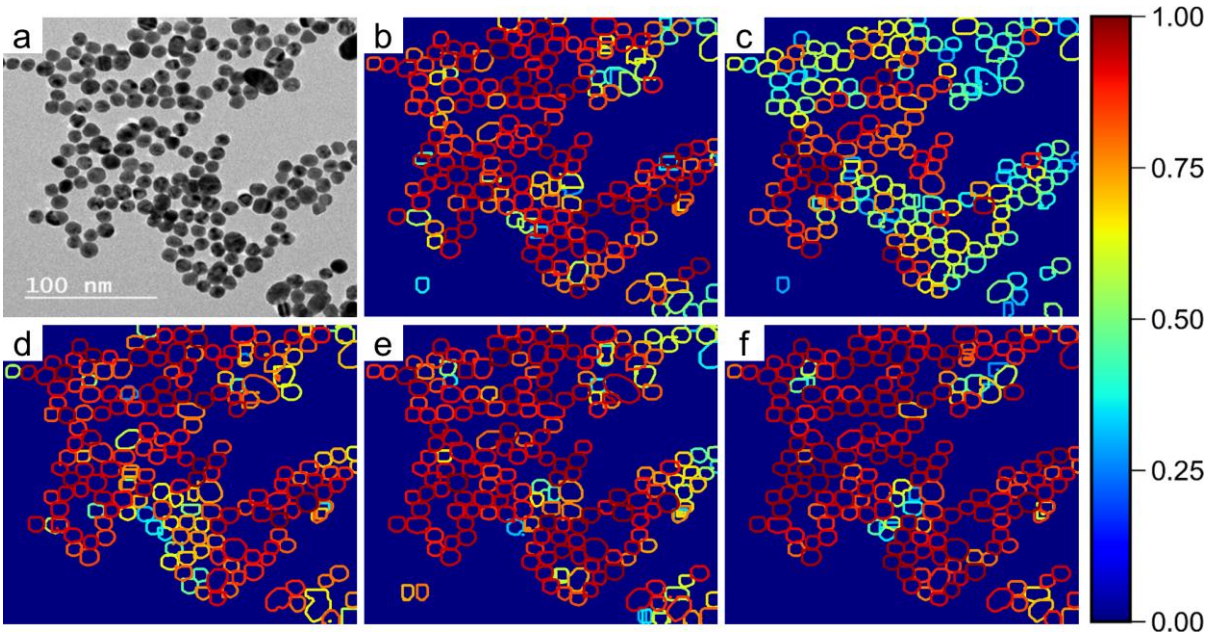

Figure S5. Visualization of instance boundary segmentation results produced by different models. **(a)** TEM image of the Cit-Au NPs [6]; **(b)** YOLOv11; **(c)** YOLOv11 with DSConv; **(d)** YOLOv11 with BADSConv; **(e)** YOLOv11 with BRA; **(f)** YOLOv11 integrating both BADSConv and BRA (NSYOLO). The color intensity indicates the boundary response strength of the predicted instances.

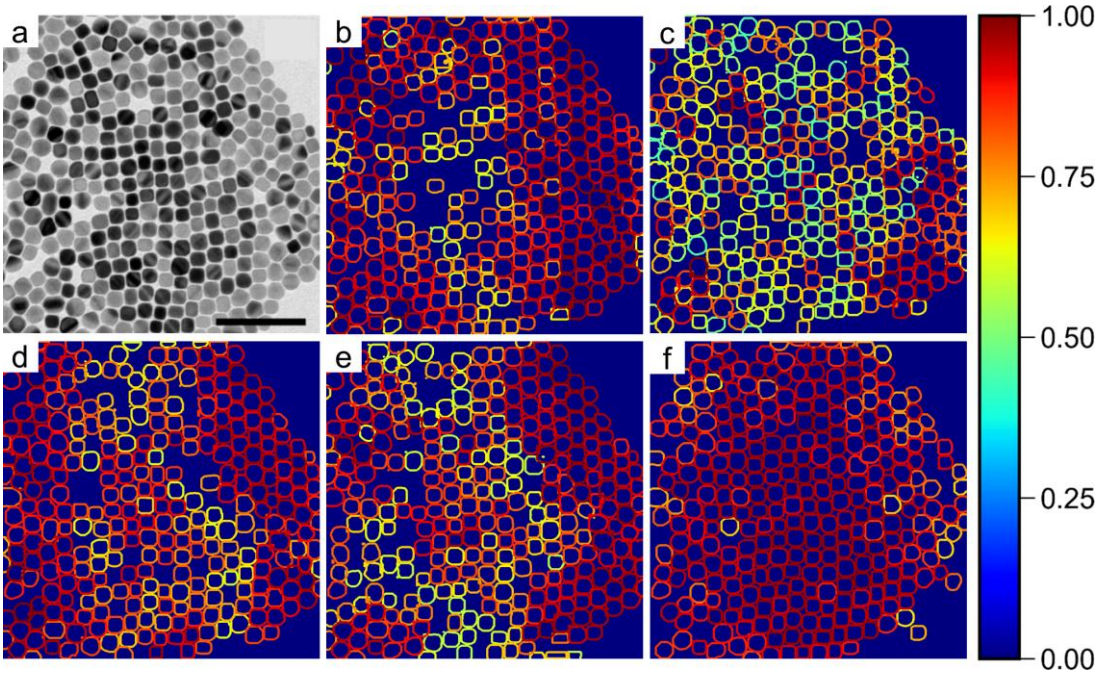

Figure S6. Visualization of instance boundary segmentation results produced by different models. **(a)** TEM image of the pristine 16 nm CuNCs [7]; **(b)** YOLOv11; **(c)** YOLOv11 with DSConv; **(d)** YOLOv11 with BADSConv; **(e)** YOLOv11 with BRA; **(f)** YOLOv11 integrating both BADSConv and BRA (NSYOLO). The color intensity indicates the boundary response strength of the predicted instances.

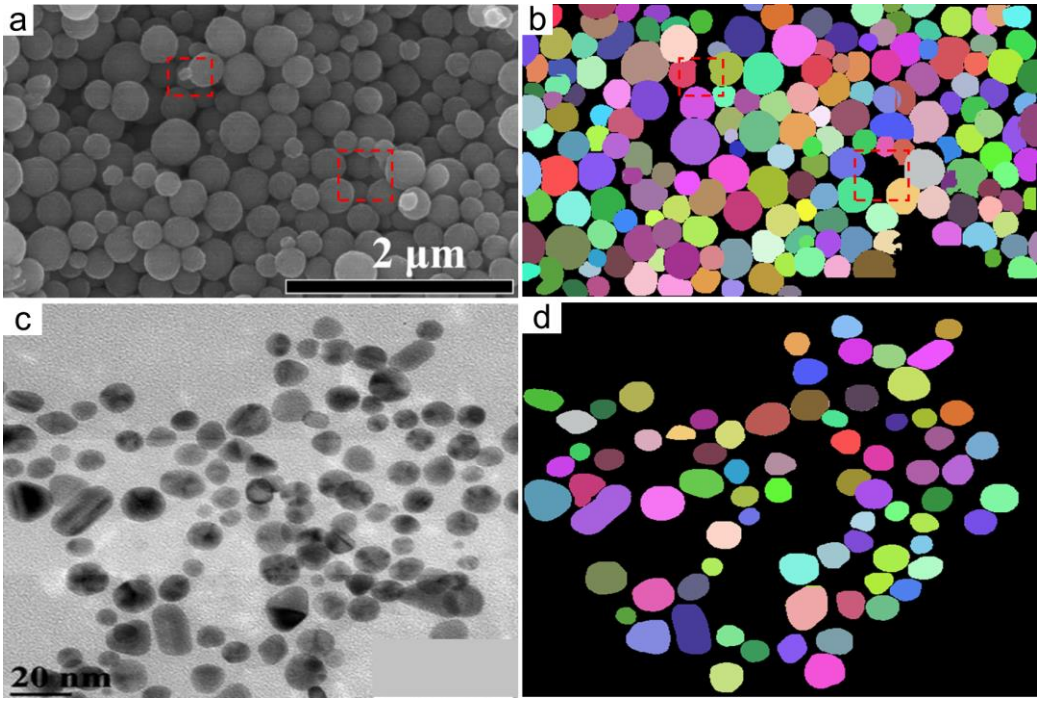

Figure S7. Segmentation results of non-ideal nanoparticles images using the NSYOLO model. **(a)** SEM image of 0.2-C@MoS_2 [8]. Reprinted with permission. Copyright 2015 American Chemical Society; **(b)** its segmentation results; **(c)** TEM image of the Au particles with different nanostructures [9]. Reprinted with permission. Copyright 2017 American Chemical Society; **(d)** its segmentation results.

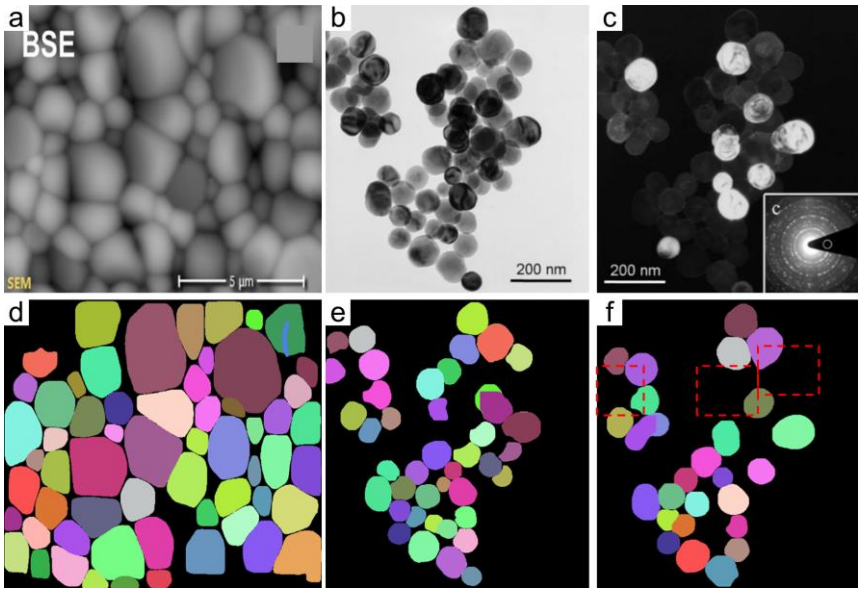

Figure S8. Segmentation performance of the NSYOLO model across different imaging modalities. **(a)** BSE-SEM image of LCMFC-IR particles [10]. Reprinted with permission. Copyright 2025 American Chemical Society; **(b)** BF-TEM and **(c)** DF-TEM images of the $BaTiO_3$ nanoparticles [11]; **(d,e,f)** Segmentation results corresponding to **(a,b,c)**, respectively.

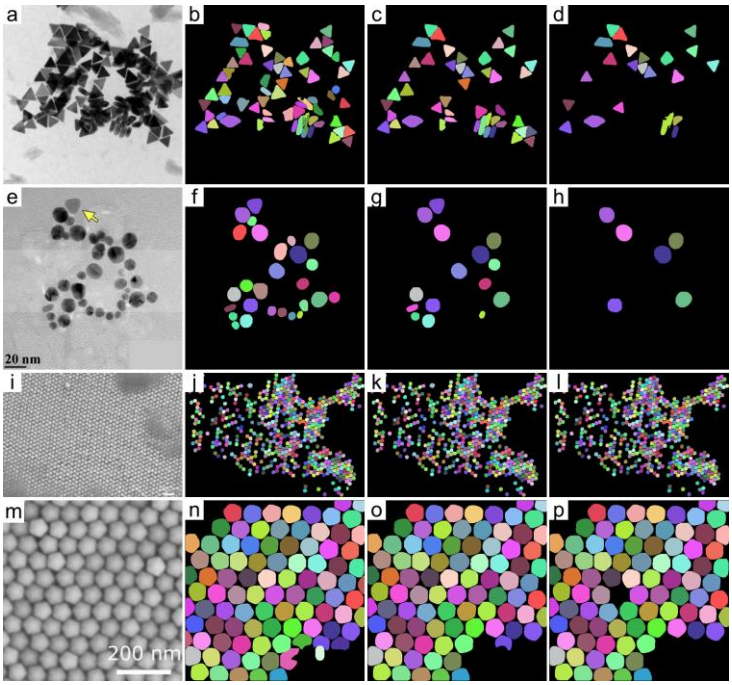

Figure S9. Segmentation results of nanoparticles with unknown morphologies at different confidence thresholds. TEM images of **(a)** the gold nanotriangles [12]. Reprinted with permission. Copyright 2017 American Chemical Society; **(e)** the gold nanostructure with mixed nanospheres and nanotriangles [9]. Reprinted with permission. Copyright 2025 American Chemical Society; SEM images of **(i)** the pentagonal nanoparticles [13] and **(m)** the rectangular arrays formed by regularly arranged pentagonal gold/silver nanoprisms [13]. Reprinted with permission. Copyright 2023 American Chemical Society; **(b–p)** Segmentation results of NSYOLO at a confidence threshold of **(b,f,j,n)** 0.25, **(c,g,k,o)** 0.5, and **(d,h,l,p)** 0.75.

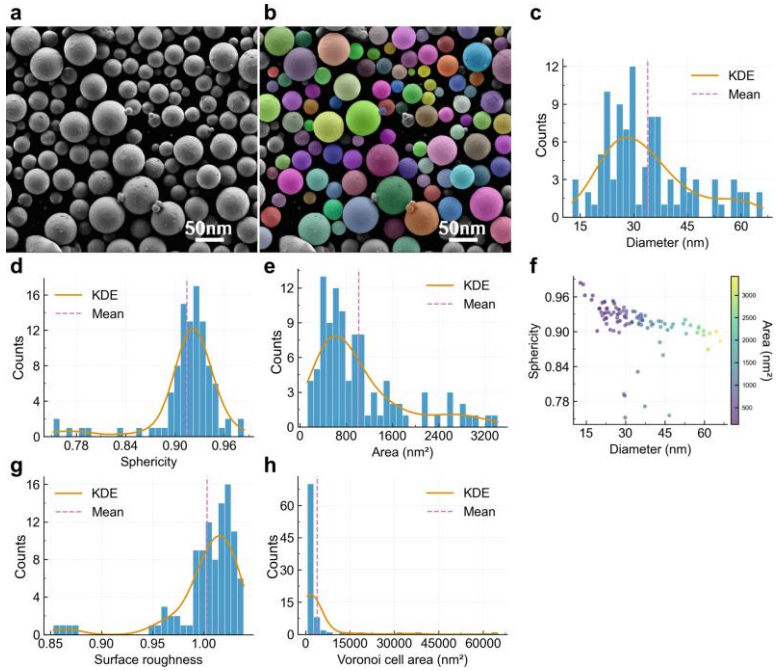

Figure S10. Comprehensive morphological characterization of spherical nanoparticles obtained from the proposed automated system: **(a)** original image; **(b)** segmentation result using the proposed method; **(c)** diameter distribution; **(d)** sphericity distribution; **(e)** area distribution; **(f)** sphericity versus diameter relationship; **(g)** surface roughness analysis; and **(h)** Voronoi area distribution. The scale bar was redrawn based on the original image for clarity.

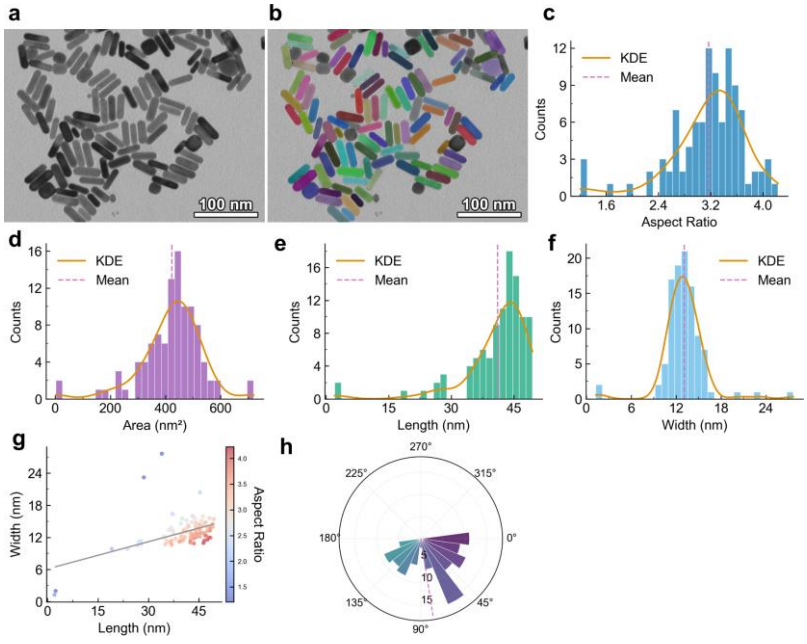

Figure S11. Comprehensive morphological characterization of nanorods obtained from the proposed automated system: **(a)** TEM image of the gold nanorods [14]. Reprinted with permission. Copyright 2015 American Chemical Society; **(b)** segmentation result using the proposed method; **(c)** aspect ratio distribution; **(d)** area distribution; **(e)** length distribution; **(f)** width distribution; **(g)** aspect ratio versus length relationship; and **(h)** orientation analysis. The scale bar was redrawn based on the original image for clarity.

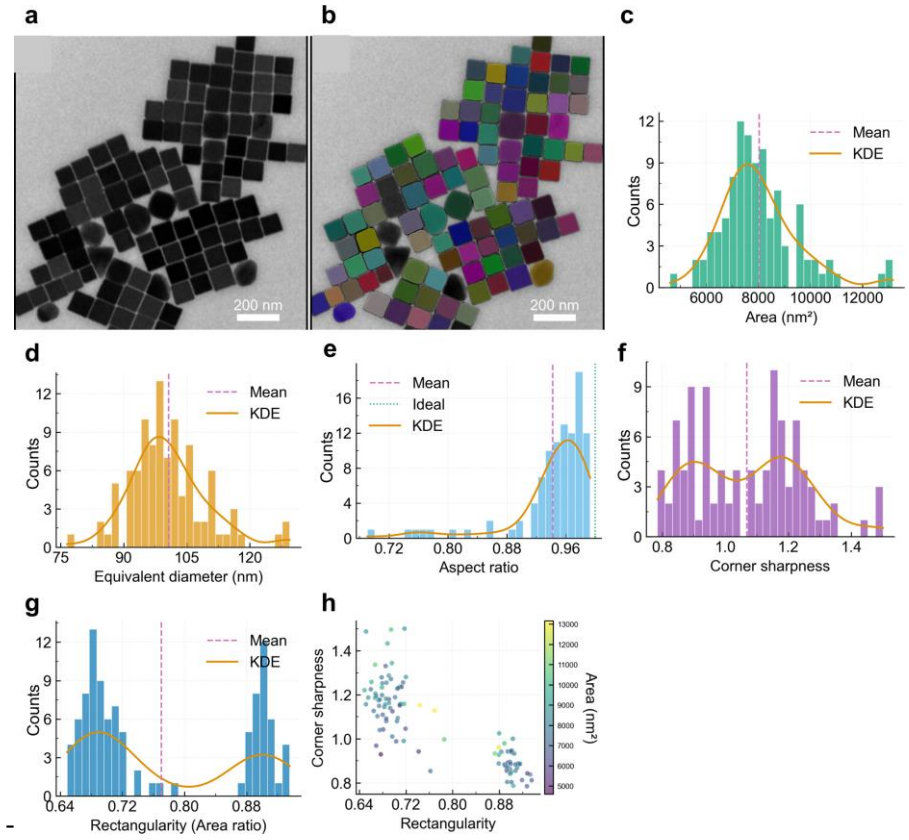

Figure S12. Comprehensive morphological characterization of nanocubes obtained from the proposed automated system: **(a)** TEM image of the nanocubes [15]; **(b)** segmentation result using the proposed method; **(c)** area distribution; **(d)** equivalent diameter distribution; **(e)** aspect ratio distribution; **(f)** corner sharpness distribution; **(g)** rectangularity distribution; and **(h)** relationship between rectangularity and corner sharpness. The scale bar was redrawn based on the original image for clarity.

2. Supplementary tables

Table S1. Ablation analysis of DSConv and the proposed BADSConv.

Method	Precision	Recall	mAP@0.5	mAP@0.5:0.95	Params (M)	GFLOPs
M1	0.885	0.882	0.906	0.696	2.98	**9.7**
M2	0.897	0.882	0.915	0.702	**2.43**	9.9
M3	**0.903**	**0.890**	**0.920**	**0.723**	2.61	10.5

Note:

M1 represents the baseline YOLOv11 model.

M2 denotes the baseline model equipped with the original DSConv module.

M3 corresponds to the proposed method, in which DSConv is further enhanced by the proposed BADSConv.

All experiments are conducted under identical training settings, and only the convolution modules are modified while the remaining network architecture is kept unchanged. The computational complexity (Params and GFLOPs) is measured using the official Ultralytics implementation by profiling a single forward pass with an input resolution of 640 × 640. The reported GFLOPs reflect the practical inference complexity and are used for relative comparison among different model variants.

Table S2. Experimental environment configuration.

Category	Specification	Description
Operating System	Ubuntu 22.04	64-bit
CPU	Intel® Xeon® Gold 6430	16 cores
GPU	NVIDIA RTX 4090	24 GB
CUDA	CUDA 12.4	GPU acceleration
Python	Python 3.10	Runtime environment
Deep Learning Framework	PyTorch 2.5.1	PyTorch version
IDE	Vscode	Development and debugging

Table S3. Model training hyperparameter settings.

Parameter	Value	Description
Input image size	640 × 640	Input image size
Epochs	100	Total training epochs
Batch size	16	Number of samples per batch
Optimizer	SGD	Stochastic Gradient Descent
Initial learning rate	0.01	Starting learning rate
Momentum	0.937	SGD momentum
Weight decay	0.0005	L2 regularization

Table S4. Detection performance on nanoparticles with non-trained morphologies under different confidence thresholds.

Confidence Threshold	Detection Rate
0.25	0.76
0.50	0.64
0.75	0.32

Note: The detection rate is defined as the ratio of correctly detected nanoparticles to the total number of nanoparticles.

References

[1] Gao Q, Pillai HS, Huang Y, Liu S, Mu Q, *et al.* Breaking adsorption-energy scaling limitations of electrocatalytic nitrate reduction on intermetallic CuPd nanocubes by machine-learned insights. *Nat. Commun.* 2022, 13(1):2338.

[2] Wei M, Deng T, Zhang Q, Cheng Z, Li S. Seed-mediated synthesis of gold nanorods at low concentrations of CTAB. *ACS Omega* 2021, 6(13):9188–9195.

[3] Wang Z, Yan X, Cong C, Xing G, Wang Z, *et al.* Green synthesis of size-controllable polyfurfuryl alcohol nanospheres as novel bio-adsorbents. *ACS Sustain. Chem. Eng.* 2023, 11(15):6032–6042.

[4] Wang Y, Zheng Y, Huang C, Xia Y. Synthesis of Ag nanocubes 18–32 nm in edge length: the effects of polyol on reduction kinetics, size control, and reproducibility. *J. Am. Chem. Soc.* 2013, 135(5):1941–1951.

[5] Khanal BP, Zubarev ER. Self-assembly of nanocrystals into ring-like superstructures: when shape, size, and material do not matter. *Langmuir* 2022, 38(12):3896–3906.

[6] Fathy MM, Elfiky AA, Bashandy YS, Hamdy MM, Elgharib AM, *et al.* An insight into synthesis and antitumor activity of citrate and gallate stabilizing gold nanospheres. *Sci. Rep.* 2023, 13(1):2749.

[7] Huang J, Hörmann N, Oveisi E, Loiudice A, De Gregorio GL, *et al.* Potential-induced nanoclustering of metallic catalysts during electrochemical CO2 reduction. *Nat. Commun.* 2018, 9(1):3117.

[8] Shao J, Qu Q, Wan Z, Gao T, Zuo Z, *et al*. From dispersed microspheres to interconnected nanospheres: carbon-sandwiched monolayered MoS2 as high-performance anode of Li-Ion batteries. *ACS Appl. Mater. Interfaces* 2015, 7(41):22927–22934.

[9] Tangeysh B, Tibbetts KM, Odhner JH, Wayland BB, Levis RJ. Gold nanotriangle formation through strong-field laser processing of aqueous kaucl4 and postirradiation reduction by hydrogen peroxide. *Langmuir* 2017, 33(1):243–252.

[10] Rosendo P, Azcondo MT, Biancotto L, Anemone G, Boulahya K, *et al*. Defects and defect association determine the actual entropy of perovskites derived from lanthanum–calcium ferrite. *Inorg. Chem.* 2025, 64(25):12446–12457.

[11] Wu H, Zhu X. *Perovskite Oxide Nanocrystals—Synthesis, Characterization, Functionalization, and Novel Applications*. London: IntechOpen, 2016.

[12] Liu W, Gupta P, Zhang Y, Thapa K, Singamaneni S, *et al.* DNA origami-assisted regioselective organization of anisotropic gold nanotriangle clusters. *ACS Appl. Opt. Mater.* 2024, 3(3):514–519.

[13] Marcone J, Chaâbani W, Goldmann C, Impéror-Clerc M, Constantin D, *et al.* Polymorphous packing of Pentagonal Nanoprisms. *Nano Lett.* 2023, 23(4):1337–1342.

[14] Xie F, Ye W, Sun H, Kou S, Guo X. Silver ions induce lateral etching of gold nanorods by K_2PtCl_4. *langmuir* 2015, 31(24):6823–6828.

[15] Huang Q, Zhang D, Yu H, Ding Y, Xia Y. Seeing is believing: how does the surface of silver nanocubes change during their growth in an aqueous system. *Nano Lett.* 2025, 25(17):7115–7120.